

Frontiers of Information Technology & Electronic Engineering
 www.jzus.zju.edu.cn; engineering.cae.cn; www.springerlink.com
 ISSN 2095-9184 (print); ISSN 2095-9230 (online)
 E-mail: jzus@zju.edu.cn



Article

The Enhanced Solution of the SVS-EFIE for Arbitrary Metal-Dielectric Composite Objects*

Han WANG, Ming-jie PANG, Hai LIN[‡]

State Key Laboratory of CAD&CG, Zhejiang University, Hangzhou, Zhejiang, China

E-mail: wanghanaviva@zju.edu.cn; mjpang@zju.edu.cn; lin@cad.zju.edu.cn

Abstract: The surface-volume-surface electric field integral equation (SVS-EFIE) can lead to complex equations, laborious implementation, and unacceptable computational complexity in the method of moments (MoM). Therefore, a general matrix equation (GME) is proposed for electromagnetic scattering from arbitrary metal-dielectric composite objects, and its enhanced solution is presented in this paper. In the previous work, the MoM solution formulation of the SVS-EFIE considering only three-region metal-dielectric composite scatters was presented, and the two-stage process resulted in two integral operators in the SVS-EFIE, which was arduous to implement and incapable of reducing computational complexity. To address these difficulties, the GME, which is versatile for homogeneous objects and composite objects consisting of more than three sub-regions, is proposed for the first time. Accelerated solving policies are proposed for the GME based on the coupling degree concerning the spacing between sub-regions, and the coupling degree standard can be adaptively set to balance the accuracy and efficiency. In this paper, the reformed addition theorem is applied for the strong coupling case, and the iterative method is presented for the weak coupling case. In addition, parallelism can be easily applied in the enhanced solution.

Key words: Composite object; Integral equation; Method of moments (MoM); Addition theorem; Iterative method

<https://doi.org/>

CLC number: TP391.4

1 Introduction

The electromagnetic (EM) simulation of metal-dielectric composite structures plays an essential role in many areas of electromagnetism such as planar microstrips, radome analysis, remote sensing, and radar applications (Lu and Chew, 2000; Lu, 2003; Xie and Li, 2018). In previous works (Poggio and Edmund, 1973; Rao et al., 1982; Ergul and Gurel, 2009), one unknown was enough for a metal object, whereas two unknowns were required to reproduce the sought field throughout a dielectric object in the surface integral equation (SIE).

Recently, the surface-volume-surface electric

field integral equation (SVS-EFIE) (Menshov and Okhmatovski, 2013; Sheikh Hosseini Lori et al., 2018) was proposed for scattering analysis of 2-D and 3-D dielectric bodies. Furthermore, the SVS-EFIE has also been applied to dielectric objects in multilayered media (Zheng et al., 2018) and metal-dielectric composite objects (Gholami and Okhmatovski, 2020). The analytic solution of the SVS-EFIE has also been presented for homogeneous dielectric spheres, which validates the rigorous nature of the SVS-EFIE (Goni and Okhmatovski, 2021). The SVS-EFIE requires only a single unknown on the boundary of the dielectric body to determine the sought field with a two-stage process (Sheikh Hosseini Lori et al., 2018). In the first stage, the unknown currents on the boundary of the scatterer are used to obtain the total field distribution throughout

[‡] Corresponding author

* Project supported by the National Key Research and Development Program (No. 2020YFC2201302)

© Zhejiang University and Springer-Verlag GmbH Germany, part of Springer Nature 2020

the volume of the scatterer. The entire field outside the scatterer is obtained in the second stage by the total field distribution throughout the volume using the volume equivalence principle. However, the two-stage process will generate two additional dense matrixes in the method of moments (MoM). Considering a metal-dielectric composite object discretized by tetrahedrons, N_v tetrahedrons in its volume and N_s triangle pairs on its boundary are observed where $N_v = N_s^\alpha$ and $\alpha \in (1, 1.5)$ (Gholami et al., 2019). In solving the SVS-EFIE using the MoM with the RWG basis function (Rao et al., 1982) and Galerkin method, N_s unknown coefficients must be determined. Apart from the normal $N_s \times N_s$ dense matrix, the first stage process leads to an additional $N_s \times N_v$ dense matrix, and the second stage process leads to an additional $N_v \times N_s$ dense matrix. The hierarchical (\mathcal{H} -) matrix has been introduced for fast analysis of the SVS-EFIE (Gholami et al., 2019). The general mathematical framework of the \mathcal{H} -matrix provides a highly compact representation of the impedance matrix, which can reduce the time and memory usage for solving the SVS-EFIE. However, the \mathcal{H} -matrix accelerated method does not consider the difference between the strong coupling and the weak coupling cases among the composite objects. Moreover, although the SVS-EFIE has been applied to metal-dielectric composite objects in Gholami and Okhmatovski (2020), only the MoM solution formulation considering three-region metal-dielectric composite scatterers is presented. Therefore, although the SVS-EFIE can efficiently reduce the number of unknowns in the SIE for dielectric scatterers, solving the SVS-EFIE using the MoM will result in complex equations, laborious implementation, and unacceptable computational complexity.

To address these problems, an enhanced solution of the SVS-EFIE for arbitrary metal-dielectric composite objects is proposed in this paper. The MoM is the core solver of the enhanced solution. In addition, CPU parallelism (Dagum and Menon, 1998; Aluru et al., 2002) can be easily applied to improve the computational efficiency of the accelerated methods. The two main contributions of this paper are as follows:

- (1) First, a general matrix equation (GME) is presented to solve the SVS-EFIE for arbitrary metal-dielectric composite objects using the MoM. The new GME is highly adaptive to ho-

mogeneous objects and composite objects that consist of more than three sub-regions. Furthermore, the GME has a simple form that is easy to implement on computers.

- (2) Second, an enhanced solution of the GME is presented. Two acceleration policies are proposed for solving the GME based on the coupling degree, which can be set adaptively to balance accuracy and efficiency. For the strong coupling case, the addition theorem, which has been widely used in computational electromagnetics, is adopted to accelerate matrix-vector multiplication (MVM) and matrix-matrix multiplication (Chew et al., 2001; Song et al., 1997). For the weak coupling case, the iterative method is adopted to consider the weak coupling among different parts, and adaptive cross approximation (ACA) (Zhao et al., 2005) is introduced to compress the coupling matrix among different sub-regions. In the enhanced solution, computational complexity is reduced to $O(N_s^\alpha \log N_s)$ where N_s is the number of total triangle pairs on the boundary of the composite object.

The rest of this paper is organized as follows: Section 2 briefly introduces the basic principle of the SVS-EFIE. The GME of the SVS-EFIE for arbitrary metal-dielectric composite objects is presented in Section 3 and the enhanced solution of the GME is presented in Section 4. Section 5 illustrates the accuracy and efficiency of the enhanced solution using several numerical results, and Section 6 presents our conclusions.

2 Basic principle of the SVS-EFIE

Consider the scattering of the time-harmonic incident field \mathbf{E}^{inc} on a homogeneous dielectric object of volume V . Using the volume equivalence principle, the electric field inside and outside the scatterer can be defined as

$$\mathbf{E}(\mathbf{r}) = \mathbf{E}^{\text{inc}}(\mathbf{r}) + k_0^2(\epsilon - 1) \int_V \overline{\mathbf{G}}_{e0}(\mathbf{r}, \mathbf{r}') \cdot \mathbf{E}(\mathbf{r}') dv' \quad (1)$$

where \mathbf{r} is the observation point in space, \mathbf{r}' is the source point inside the scatterer, ϵ is the complex relative permittivity, $k_0 = \omega \sqrt{\epsilon_0 \mu_0}$ is the wavenum-

ber of vacuum, and ϵ_0 , μ_0 are permittivity and permeability of vacuum, respectively. The 3-D dyadic Green's function of free space is

$$\bar{\bar{G}}_{e0}(\mathbf{r}, \mathbf{r}') = \left(\frac{\nabla \nabla}{k_0^2} + \bar{I} \right) \frac{e^{-ik_0|\mathbf{r}-\mathbf{r}'|}}{4\pi|\mathbf{r}-\mathbf{r}'|} \quad (2)$$

where \bar{I} is the idem-factor.

By the homogeneous wave equation, the total electric field inside the scatterer V satisfies

$$\nabla \times \nabla \times \mathbf{E}(\mathbf{r}) - k_\epsilon^2 \mathbf{E}(\mathbf{r}) = 0, \mathbf{r} \in V \setminus \partial V. \quad (3)$$

It can be written as a superposition of spherical waves emanating from object boundary ∂V as

$$\mathbf{E}(\mathbf{r}) = -i\omega\mu_0 \int_{\partial V} \bar{\bar{G}}_{e\epsilon}(\mathbf{r}, \mathbf{r}') \cdot \mathbf{J}(\mathbf{r}') ds', \mathbf{r} \in V \setminus \partial V \quad (4)$$

where $k_\epsilon = k_0\sqrt{\epsilon}$ is the wavenumber inside the homogeneous non-magnetic medium, and the 3-D dyadic Green's function is

$$\bar{\bar{G}}_{e\epsilon}(\mathbf{r}, \mathbf{r}') = \left(\frac{\nabla \nabla}{k_\epsilon^2} + \bar{I} \right) \frac{e^{-ik_\epsilon|\mathbf{r}-\mathbf{r}'|}}{4\pi|\mathbf{r}-\mathbf{r}'|}. \quad (5)$$

Substituting Eq. (4) into Eq. (1), and restricting the observation domain to the surface of the scatterer, yields the SVS-EFIE (Sheikh Hosseini Lori et al., 2018)

$$\begin{aligned} \hat{\mathbf{t}} \cdot \mathbf{E}^{\text{inc}}(\mathbf{r}) &= i\omega\mu_0 \hat{\mathbf{t}} \cdot \left(- \int_{\partial V} \bar{\bar{G}}_{e\epsilon}(\mathbf{r}, \mathbf{r}'') \cdot \mathbf{J}(\mathbf{r}'') ds'' \right. \\ &+ k_0^2(\epsilon - 1) \int_V \bar{\bar{G}}_{e0}(\mathbf{r}, \mathbf{r}') \\ &\quad \cdot \oint_{\partial V} \bar{\bar{G}}_{e\epsilon}(\mathbf{r}', \mathbf{r}'') \cdot \mathbf{J}(\mathbf{r}'') ds'' dv', \\ &\quad \left. \mathbf{r} \in \partial V \right) \end{aligned} \quad (6)$$

where $\hat{\mathbf{t}}$ is the tangential vector to the surface ∂V .

3 The GME of the SVS-EFIE for composite objects

The SVS-EFIE was extended to the SVS-S-EFIE for composite conductor-dielectric materials by Gholami and Okhmatovski (2020), but only the

MoM solution formulation for three-region composite objects was presented. Here, we present a general solution form of the SVS-EFIE based on the MoM for arbitrary metal-dielectric composite objects. Homogeneous objects and composite objects consisting of more than three sub-regions can be easily expanded from the GME.

Consider an arbitrary metal-dielectric composite object that consists of P_c conductor regions and P_d dielectric regions. The index range of the metal regions is from 1 to P_c and the index range of dielectric regions is from $P_c + 1$ to $P_c + P_d$. By the equivalence principle and enforcement of the vanishing tangential electric field on the surface of the metal region, the sum of the tangential part of the incident field and the total scattered field generated from all sub-regions of the composite objects on the metal region surface equals zero. By the volume-surface equivalence principle (Lu and Chew, 2000; Xie and Li, 2018) and restricting the observation point to the boundary of the dielectric region, the tangential part of the total field of the dielectric region's boundary is equal to the sum of the incident field of the region and scattered field generated from all sub-regions of the composite objects. Adjusting these pieces of information, the extended SVS-EFIE for composite objects can be represented as

$$\hat{\mathbf{t}}_p \cdot \mathbf{E}_p^{\text{inc}}(\mathbf{r}_p) = -\hat{\mathbf{t}}_p \cdot \sum_{q=1}^{P_c+P_d} \mathbf{E}_q^{\text{sca}}(\mathbf{r}_p), \quad (7)$$

$$\mathbf{r}_p \in \partial V_p, p \in [1, P_c]$$

$$\hat{\mathbf{t}}_p \cdot \mathbf{E}_p^{\text{inc}}(\mathbf{r}_p) = \hat{\mathbf{t}}_p \cdot (\mathbf{E}_p(\mathbf{r}_p) - \sum_{q=1}^{P_c+P_d} \mathbf{E}_q^{\text{sca}}(\mathbf{r}_p)), \quad (8)$$

$$\mathbf{r}_p \in \partial V_p, p \in [P_c + 1, P_c + P_d]$$

where $\mathbf{E}_p^{\text{inc}}$ is the incident field of the region p , $\mathbf{E}_q^{\text{sca}}$ is the scattering field generated by region q , \mathbf{E}_p is the total field of the dielectric region p , \mathbf{r}_p is the observation point on the boundary of the region p , $\hat{\mathbf{t}}_p$ is the tangential vector to the boundary of the region p and ∂V_p is the boundary of the region p . Moreover, using Eq. (4), the total field of the dielectric region p is

$$\mathbf{E}_p(\mathbf{r}_p) = -i\omega\mu_0 \int_{\partial V_p} \bar{\bar{G}}_{e\epsilon_p}(\mathbf{r}, \mathbf{r}') \cdot \mathbf{J}_p(\mathbf{r}') ds', \quad (9)$$

$$\mathbf{r} \in V_p \setminus \partial V_p, \mathbf{r}_p \in \partial V_p, p \in [P_c + 1, P_c + P_d]$$

$$\mathbf{E}_q^{\text{sca}}(\mathbf{r}) = \begin{cases} -i\omega\mu_0 \oint_{\partial V_q} \bar{\bar{G}}_{e0}(\mathbf{r}, \mathbf{r}'_q) \cdot \mathbf{J}_q(\mathbf{r}'_q) ds', \mathbf{r}'_q \in \partial V_q, q \in [1, P_c] \\ -i\omega\mu_0 k_0^2(\epsilon - 1) \int_{V_q} \bar{\bar{G}}_{e0}(\mathbf{r}, \mathbf{r}'_q) \cdot \oint_{\partial V_q} \bar{\bar{G}}_{e\epsilon_q}(\mathbf{r}'_q, \mathbf{r}''_q) \cdot \mathbf{J}_q(\mathbf{r}''_q) ds'' dv', q \in [P_c + 1, P_c + P_d] \end{cases} \quad (11)$$

where \mathbf{J}_p is the unknown equivalent currents on the boundary of the region p . The Green's function of the dielectric region p is

$$\bar{\bar{G}}_{e\epsilon_p}(\mathbf{r}, \mathbf{r}') = \left(\frac{\nabla \nabla}{k_{\epsilon_p}^2} + \bar{\bar{I}} \right) \frac{e^{-ik_{\epsilon_p}|\mathbf{r}-\mathbf{r}'|}}{4\pi|\mathbf{r}-\mathbf{r}'|}. \quad (10)$$

By the surface equivalence principle and Eq. (6), the scattered field from different sub-regions can be represented using Eq. (11), where \mathbf{r} is the observation point in free space, \mathbf{J}_q is the unknown equivalent currents on the boundary of the region q , ∂V_q is the boundary of the metal region q , V_q is the volume of the dielectric part q , ∂V_q is the boundary of the dielectric region q , and ϵ_q is the complex relative permittivity of the dielectric region q .

Combining Eqs (7)-(9), and (11) produces the general form of the SVS-EFIE for composite conductor-dielectric materials. In solving the equations using the MoM, the surfaces of metal regions are discretized by triangles, and the volumes of dielectric regions are discretized by tetrahedrons. The unknown currents \mathbf{J}_q defined on the boundary ∂V_q of the region q can be performed using the RWG basis function (Rao et al., 1982), which is defined as

$$\mathbf{f}_n(\mathbf{r}) = \begin{cases} \frac{\mathbf{r}-\mathbf{v}_n^+}{2A_n^+} & \mathbf{r} \in S_n^+ \\ \frac{\mathbf{v}_n^--\mathbf{r}}{2A_n^-} & \mathbf{r} \in S_n^- \end{cases} \quad (12)$$

where \mathbf{v}_n^\pm is the vertex that is opposite to the interior edge and A_n^\pm is the area of triangle S_n^\pm as illustrated in Fig.1, respectively. Using the Galerkin method, the GME can be written as

$$V^p = \sum_{q=1}^{P_c} Z_{SS}^{pq} I^q - \sum_{q=P_c+1}^{P_c+P_d} Z_{SVS}^{pq} I^q, p \in [1, P_c] \quad (13)$$

$$V^p = Z_{SS}^p I^p - \sum_{q=1}^{P_c} Z_{SS}^{pq} I^q - \sum_{q=P_c+1}^{P_c+P_d} Z_{SVS}^{pq} I^q, \quad (14)$$

$p \in [P_c + 1, P_c + P_d]$

where V^p is the excitation matrix related to the left part in Eqs (7) and (8). I^p and I^q are the unknown

surface current coefficients of the regions p and q , respectively. The dielectric surface-to-surface integral matrix Z_{SS}^p is generated from Eq. (9), and the matrix elements are computed by

$$\begin{aligned} Z_{SS}^p(m, n) &= -i\omega\mu_0 \int_{\mathbf{f}_m} \mathbf{f}_m(\mathbf{r}) \cdot \int_{\mathbf{f}_n} \bar{\bar{G}}_{e\epsilon_p}(\mathbf{r}, \mathbf{r}') \cdot \mathbf{f}_n(\mathbf{r}') d\mathbf{r}' d\mathbf{r}, \\ \mathbf{f}_n &\in \partial V_p, \mathbf{f}_m \in \partial V_p, p \in [P_c + 1, P_c + P_d]. \end{aligned} \quad (15)$$

The metal surface-to-surface integral matrix Z_{SS}^{pq} is related to the surface to surface integral Eq. (11) from conductor part p to part q , and the matrix elements are calculated by

$$\begin{aligned} Z_{SS}^{pq}(m, n) &= -i\omega\mu_0 \int_{\mathbf{f}_m} \mathbf{f}_m(\mathbf{r}) \cdot \int_{\mathbf{f}_n} \bar{\bar{G}}_{e0}(\mathbf{r}, \mathbf{r}') \cdot \mathbf{f}_n(\mathbf{r}') d\mathbf{r}' d\mathbf{r}, \\ \mathbf{f}_n &\in \partial V_q, \mathbf{f}_m \in \partial V_p, q \in [1, P_c]. \end{aligned} \quad (16)$$

The dielectric surface-volume-surface integral matrix Z_{SVS}^{pq} is related to the SVS integral Eq. (11) from dielectric part p to part q , and the matrix elements are computed by

$$\begin{aligned} Z_{SVS}^{pq}(m, n) &= -i\omega\mu_0 k_0^2(\epsilon - 1) \int_{\mathbf{f}_m} \mathbf{f}_m(\mathbf{r}) \cdot \int_{V_q} \bar{\bar{G}}_{e0}(\mathbf{r}, \mathbf{r}'_q) \\ &\quad \cdot \oint_{\mathbf{f}_n} \bar{\bar{G}}_{e\epsilon_q}(\mathbf{r}'_q, \mathbf{r}''_q) \cdot \mathbf{f}_n(\mathbf{r}''_q) d\mathbf{r}'_q dv', \\ \mathbf{f}_n &\in \partial V_q, \mathbf{f}_m \in \partial V_p, q \in [P_c + 1, P_c + P_d]. \end{aligned} \quad (17)$$

The excitation matrix is calculated by

$$V^p(m) = \int_{\mathbf{f}_m} E^{\text{inc}}(\mathbf{r}) \cdot \mathbf{f}_m(\mathbf{r}) d\mathbf{r}, \mathbf{f}_m \in \partial V_p. \quad (18)$$

In Eqs (15)-(20), \mathbf{f}_m is the RWG test function and \mathbf{f}_n is the RWG basis function. To handle the three integral operators in Eq. (17), we hypothesize that the total field varies slowly enough to be approximated within each tetrahedron by their values at the centroid of the tetrahedron. Thus, the $N_s^p \times N_s^q$ matrix Z_{SVS}^{pq} can be written as the multiplication of a $N_s^p \times N_v^q$ matrix Z_{SV} and a $N_v^q \times N_s^q$ matrix Z_{VS} , where

$$\begin{aligned} Z_{SV}(m, n_t) &= k_0^2(\epsilon - 1) \int_{\mathbf{f}_m} \mathbf{f}_m(\mathbf{r}) \\ &\cdot \int_{V_q^{n_t}} \overline{G}_{e0}(\mathbf{r}, \mathbf{r}') \\ &\cdot [g_{n_t}^x(\mathbf{r}') \ g_{n_t}^y(\mathbf{r}') \ g_{n_t}^z(\mathbf{r}')]^T dv d\mathbf{r}', \\ &\mathbf{f}_m \in \partial V_p, V_q^{n_t} \in V_q \end{aligned} \quad (19)$$

and

$$\begin{aligned} Z_{VS}^{x,y,z}(n_t, n) &= \left(-i\omega\mu_0 \int_{\mathbf{f}_n} \overline{G}_{eeq}(\mathbf{r}', \mathbf{r}'') \cdot \mathbf{f}_n(\mathbf{r}'') d\mathbf{r}'' \right)_{x,y,z}, \quad (20) \\ &\mathbf{r}' \text{ is the centroid of } V_q^{n_t}. \end{aligned}$$

Note that the integral in Eq. (20) results in a vector, and the x, y, and z components are stored separately in Z_{VS}^x , Z_{VS}^y , and Z_{VS}^z . $g_{n_t}^{x,y,z}(\mathbf{r})$ is the volume pulse-function defined on the tetrahedron element $V_q^{n_t}$ as

$$g_{n_t}^{x,y,z}(\mathbf{r}) = \begin{cases} 1 & \mathbf{r} \in V_q^{n_t} \\ 0 & \mathbf{r} \notin V_q^{n_t} \end{cases}. \quad (21)$$

4 Enhanced solution of the GME

The GME of the SVS-EFIE can be solved directly, but the computational complexity of the direct solution is unacceptable in practical applications. The dielectric and metal surface-to-surface integral matrixes in Eqs (13) and (14) require $O(N_s^2)$ memory storage. In addition, the two dense matrixes in Eqs (19) and (20) require $O(N_s N_v)$ memory storage. The surface-volume-surface integral matrix is generated by the multiplication of two dense matrixes, leading to time complexity of $O(N_s^2 N_v)$. In addition, the direct matrix equation solver for the

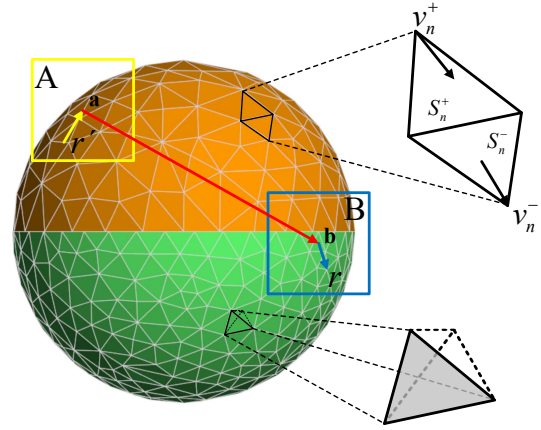


Fig. 1 Illustration of mesh, basis functions, and wave translation. (1) Mesh: The metal region of the model, colored in orange, is discretized by triangle pairs, and the dielectric region of the model, colored in green, is discretized by tetrahedrons. (2) Basis functions: The RWG basis function represents the equivalent currents on the boundary of each region. The RWG basis function is defined on the triangle pairs. (3) Wave translation: For clarity, a square represents a group (cube). Groups A and B in the same layer are marked as relatively far groups for each other. a and b are geometric centers of the two groups, \mathbf{r}' is the source point, and \mathbf{r} is the observation point. The yellow arrow represents the upward aggregation, the red arrow represents the translation, and the blue arrow represents the downward disaggregation. Fields in group A are first aggregated to the point a . Then the field at point a is translated to all the relatively far groups of group A. All received fields at point b are finally disaggregated to child cubes or basis functions in the group B.

GME requires $O(N_s^3)$ CPU time. Therefore, given that $N_v = N_s^\alpha$ and $\alpha \in (1, 1.5)$, the direct solution of the GME has $O(N_s^{1+\alpha})$ space complexity and $O(N_s^{2+\alpha})$ time complexity.

In this paper, an enhanced solution of the general form is presented to reduce computational complexity. Two policies are presented based on the coupling degree concerning the spacing between different sub-regions. For the strong coupling case, the coupling matrixes between two sub-regions contribute significantly to the final result. Thus, the coupling matrixes should be stored explicitly, and the physical considerations such as the addition theorem are suitable for reducing the computational complexity. For the weak coupling case, the coupling matrixes between two sub-regions have a weak influence on the final result. Thus, the coupling matrixes can be compressed by an algebraic method such as ACA,

and the iterative method is suitable for considering the weak coupling.

4.1 Enhanced solution for the strong coupling case

In this paper, the method based on the addition theorem is proposed to solve the composite objects of the strong coupling case. Applying the addition algorithm to the Green's function in Eqs (2) and (10) yields

$$\begin{aligned} \bar{G}_{e0, \epsilon_q}(\mathbf{r}, \mathbf{r}') &= \left(\bar{I} - \frac{\nabla \nabla'}{k_{0, \epsilon_q}^2} \right) \frac{e^{-ik_{0, \epsilon_q} |\mathbf{r} - \mathbf{r}'|}}{4\pi |\mathbf{r} - \mathbf{r}'|} \\ &= \frac{1}{4\pi} \int [\bar{I} - \hat{\mathbf{k}} \hat{\mathbf{k}}] e^{-ik_{0, \epsilon_q} \hat{\mathbf{k}} \cdot (\mathbf{r}_{rb} - \mathbf{r}_{r'a})} \\ &\quad T_L(k_{0, \epsilon_q}, \hat{\mathbf{k}}, \mathbf{r}_{ba}) d^2 \hat{\mathbf{k}}, \\ &\quad |\mathbf{r}_{ba}| < |\mathbf{r}_{rb}| + |\mathbf{r}_{r'a}| \end{aligned} \quad (22)$$

and

$$\begin{aligned} T_L(k_{0, \epsilon_q}, \hat{\mathbf{k}}, \mathbf{r}_{ba}) &= \frac{k}{4\pi} \sum_{l=0}^L (-i)^{l+1} (2l+1) h_l^{(2)}(k_{0, \epsilon_q} |\mathbf{r}_{ba}|) P_l(\hat{\mathbf{k}} \cdot \hat{\mathbf{r}}_{ba}) \\ &\quad (23) \end{aligned}$$

$$\begin{aligned} \mathbf{r} - \mathbf{r}' &= (\mathbf{r} - \mathbf{b}) + (\mathbf{b} - \mathbf{a}) - (\mathbf{r}' - \mathbf{a}) \\ &= \mathbf{r}_{rb} + \mathbf{r}_{ba} - \mathbf{r}_{r'a} \end{aligned} \quad (24)$$

where \mathbf{r}' is the source point, \mathbf{r} is the observation point as illustrated in Fig.1, and \mathbf{a} , \mathbf{b} are vectors obtained by adding a small offset to \mathbf{r}' and \mathbf{r} , respectively. $P_l(x)$ is a Legendre polynomial of order l , $h_l^{(2)}(x)$ is a spherical Hankel function of the second kind, and L is the truncation order.

Applying the addition theorem to the four matrix elements shown in Section 3 produces new formulas to calculate the elements that satisfy the constraint in Eq. (22).

- (1) Applying the addition theorem to Eq. (15), the V_{SS}^p element can be written as

$$\begin{aligned} Z_{SS}^p(m, n) &= -\frac{i\omega\mu_0}{4\pi} \int \mathbf{R}_{s\epsilon_p}(\hat{\mathbf{k}}) \cdot T_L(k_{\epsilon_q}, \hat{\mathbf{k}}, \mathbf{r}_{ba}) \mathbf{T}_{s\epsilon_p}(\hat{\mathbf{k}}) d^2 \hat{\mathbf{k}} \\ &\quad (25) \end{aligned}$$

where the radiation function is

$$\mathbf{T}_{s\epsilon_p}(\hat{\mathbf{k}}) = [\bar{I} - \hat{\mathbf{k}} \hat{\mathbf{k}}] \cdot \int_{f_n} e^{ik_{\epsilon_p} \hat{\mathbf{k}} \cdot \hat{\mathbf{r}}_{r'a}} \mathbf{f}_n(\mathbf{r}') d\mathbf{r}' \quad (26)$$

and the receive function is

$$\mathbf{R}_{s\epsilon_p}(\hat{\mathbf{k}}) = [\bar{I} - \hat{\mathbf{k}} \hat{\mathbf{k}}] \cdot \int_{f_m} e^{-ik_{\epsilon_p} \hat{\mathbf{k}} \cdot \hat{\mathbf{r}}_{rb}} \mathbf{f}_m(\mathbf{r}) d\mathbf{r}. \quad (27)$$

- (2) Applying the addition theorem to Eq. (16), the V_{SS}^{pq} element can be written as

$$\begin{aligned} Z_{SS}^{pq}(m, n) &= -\frac{i\omega\mu_0}{4\pi} \int \mathbf{R}_{s0}(\hat{\mathbf{k}}) \cdot T_L(k_0, \hat{\mathbf{k}}, \mathbf{r}_{ba}) \mathbf{T}_{s0}(\hat{\mathbf{k}}) d^2 \hat{\mathbf{k}} \\ &\quad (28) \end{aligned}$$

where the radiation function is

$$\mathbf{T}_{s0}(\hat{\mathbf{k}}) = [\bar{I} - \hat{\mathbf{k}} \hat{\mathbf{k}}] \cdot \int_{f_n} e^{ik_0 \hat{\mathbf{k}} \cdot \hat{\mathbf{r}}_{r'a}} \mathbf{f}_n(\mathbf{r}') d\mathbf{r}' \quad (29)$$

and the receive function is

$$\mathbf{R}_{s0}(\hat{\mathbf{k}}) = [\bar{I} - \hat{\mathbf{k}} \hat{\mathbf{k}}] \cdot \int_{f_m} e^{-ik_0 \hat{\mathbf{k}} \cdot \hat{\mathbf{r}}_{rb}} \mathbf{f}_m(\mathbf{r}) d\mathbf{r}. \quad (30)$$

- (3) Applying the addition theorem to Eq. (19), the element can be written as

$$\begin{aligned} Z_{SV}(m, n_t) &= -\frac{k_0^2(\epsilon - 1)}{4\pi} \int \mathbf{R}_{s0}(\hat{\mathbf{k}}) \cdot T_L(k_{\epsilon_q}, \hat{\mathbf{k}}, \mathbf{r}_{ba}) \\ &\quad [T_{v0}^x(\hat{\mathbf{k}}) \quad T_{v0}^y(\hat{\mathbf{k}}) \quad T_{v0}^z(\hat{\mathbf{k}})]^T d^2 \hat{\mathbf{k}} \end{aligned} \quad (31)$$

where the radiation function in the volume-to-surface integral process is

$$T_{v0}^{x,y,z}(\hat{\mathbf{k}}) = e^{ik_0 \hat{\mathbf{k}} \cdot \hat{\mathbf{r}}_{r'a}} \quad (32)$$

and the receive function that is defined on the RWG basis functions on the boundary of the scatterer is the same as Eq. (30).

- (4) Applying the addition theorem to Eq. (20), the Z_{VS} element can be written as

$$\begin{aligned} Z_{VS}^{x,y,z}(n_t, n) &= -\frac{i\omega\mu_0}{4\pi} \int R_{v\epsilon_p}(\hat{\mathbf{k}}) T_L(k_{\epsilon_q}, \hat{\mathbf{k}}, \mathbf{r}_{ba}) \mathbf{T}_{s\epsilon_p}(\hat{\mathbf{k}}) d^2 \hat{\mathbf{k}} \\ &\quad (33) \end{aligned}$$

where the element of the radiation function is the same as Eq. (26), and the receive function in tetrahedron's volume is

$$R_{v\epsilon_p}(\hat{\mathbf{k}}) = e^{-ik_{\epsilon_p} \hat{\mathbf{k}} \cdot \hat{\mathbf{r}}_{rb}}. \quad (34)$$

The addition theorem can accelerate the MVM in the iterative solver for matrix equations such as the Jacobi method, Gauss-Seidel method, and conjugate gradient method. The MVM based on the addition theorem has three main steps.

First, the tree-based Octree subdivision scheme is used to divide the RWG triangle pairs and tetrahedrons into layered cubes (groups) (Meagher, 1982). In the Octree subdivision scheme, the entire object is enclosed in a large cube, which is then partitioned into eight child cubes. Each child cube is then recursively subdivided into eight smaller cubes as long as the edge length of the finest cube is no less than the threshold (0.25λ in this paper where λ is the wavelength). As shown in Fig.1, a cube (group) can contain only RWG triangle pairs from a single region (group A) or RWG triangle pairs of different sub-regions and tetrahedrons (group B).

Second, for a cube in each layer, other cubes are marked as the near group, the relatively far group, and the far group based on their positions. If cube C_2 adjoins cube C_1 , then C_2 is marked as a near group of C_1 . If cube C_3 does not adjoin C_1 , but their parent cubes are adjoined, then C_3 is marked as a relatively far group of C_1 . Other cubes in the same layer are marked as far groups of C_1 .

Third, the corresponding near-group impedance elements in the finest layer are computed by conventional MoM and stored explicitly. The MVM related to the relatively far group in each layer is accelerated by the addition theorem. Thus, the calculations of V_{SS}^p , V_{SS}^{pq} , V_{SV} and V_{VS} are accelerated through three processes: upward aggregation, translation, and downward disaggregation, as illustrated in Fig.1. For each basis function in the finest layer, the aggregated field to the center of its parent group is calculated by the radiation functions, and its disaggregated field is directly calculated by the receive functions. For each cube, the aggregated field to the center of its parent group is aggregated and interpolated, and the disaggregated field is antinterpolated and disaggregated from the center of its parent group (Bucci et al., 1991; Chew et al., 2001; Sarvas, 2003). Note that the interpolation and antinterpolation are required due to the different sampling rates in different layers when we calculate the integral in Eq. (22).

In the enhanced solution for the strong coupling case, an Octree structure with $O(\log(N_s))$ layers will be constructed. In each layer, the aggregation, trans-

lation, and disaggregation processes require $O(N_v)$ memory storage and CPU time (Song and Chew, 1995). Thus, the enhanced solution for the strong coupling case has $O(N_s^\alpha \log(N_s))$ computational complexity.

4.2 Enhanced solution for the weak coupling case

Considering a composite conductor-dielectric object whose spacing among different homogeneous sub-regions is relatively far (no less than 0.1λ in this paper), the coupling among different sub-regions has a weak influence on the final result. Thus, we propose an iterative method to solve the GME with weak coupling in this paper. The flowchart of the iterative method is illustrated in Fig.2. There are two main processes: the inner solving process and the iteration process. Details of the two processes will be presented in the following subsections.

4.2.1 Inner solving process

In the inner solving process, the Octree structure and the addition theorem are used in each homogeneous region as illustrated in Section 4.1. After the incident field is determined, different homogeneous parts are solved independently. In this implementation, the inner solver of the conductor parts solves

$$V_i^p = Z_{SS}^{pp} I^p, p \in [1, P_c] \quad (35)$$

and the inner solver of the homogeneous dielectric parts solves

$$V_i^p = Z_{SS}^{pp} I^p - Z_{SVS}^{pp} I^p, p \in [P_c + 1, P_c + P_d] \quad (36)$$

where V_i^p is the excitation vector of the region p in the i^{th} iteration process.

4.2.2 Iteration process

The coupling among different sub-regions is considered in the iteration process. In each iteration process, an additional excitation matrix ΔV^p is computed for each region, and the excitation matrix of region p in the $(i + 1)^{th}$ iteration is calculated by

$$V_{i+1}^p = V_0^p + \Delta V_{i+1}^p \quad (37)$$

where

$$\Delta V_{i+1}^p = \sum_{q=1}^{P_c, q \neq p} Z_{SS}^{pq} I_i^q + \sum_{q=P_c+1}^{P_c+P_d} Z_{SVS}^{pq} I_i^q, p \in [1, P_c] \quad (38)$$

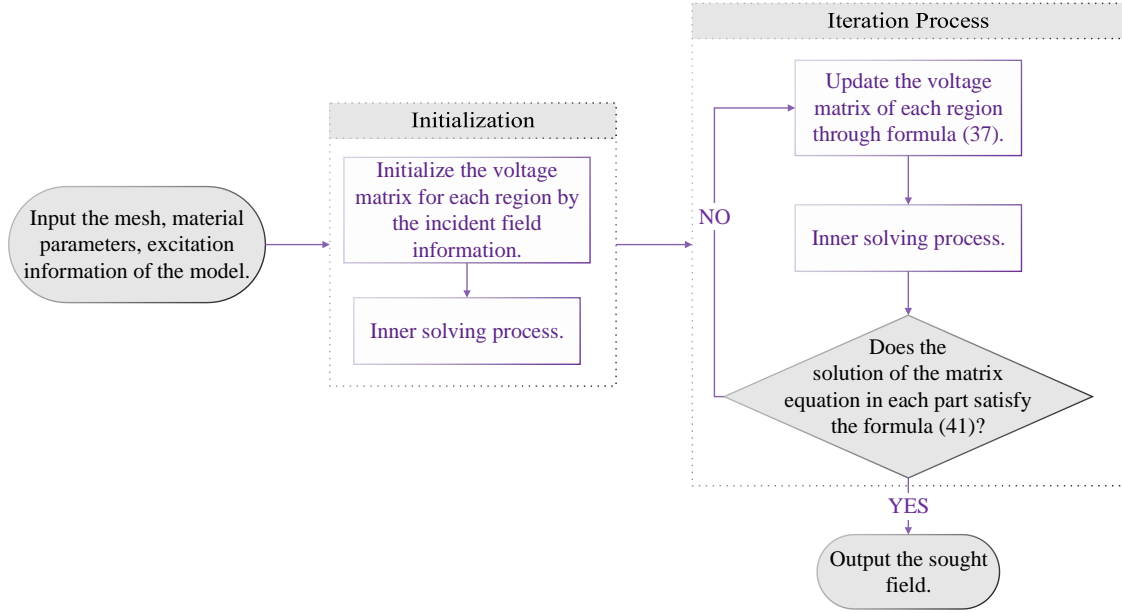


Fig. 2 General flowchart of the enhanced solution for the weak coupling case.

and

$$\Delta V_{i+1}^p = \sum_{q=1}^{P_c} Z_{SS}^{pq} I_i^q + \sum_{q=P_c+1}^{P_c+P_d, q \neq p} Z_{SV}^{pq} I_i^q, \quad (39)$$

$$p \in [P_c + 1, P_c + P_d].$$

In Eqs (38) and (39), I_i^q is the current vector matrix of part q gained in the i^{th} iteration process and V_0^p is the same as Eq. (18). Due to the weak coupling among different sub-regions, the coupling matrices are low-rank. The ACA (Zhao et al., 2005) can be used to compress the coupling matrices. Thus, the low-rank coupling impedance matrixes in equation Eqs (38) and (39) can be compressed by

$$\tilde{Z}^{m \times n} \approx (U^{m \times r} V^{r \times n}) \quad (40)$$

where r is the effective rank of the $m \times n$ weak coupling matrix Z ($r \ll m, n$), and the $m \times r$ matrix U and $r \times n$ matrix V are two dense rectangular matrices.

The iteration process will stop when the current becomes stable, and the stopping criterion is

$$\frac{\|I_p^{i+1} - I_p^i\|}{\|I_p^i\|} < \xi \quad (41)$$

where the norm is defined as the 2-norm form, and ξ is the threshold value.

In the enhanced solution for the weak coupling case, the coupling among different sub-regions is accelerated by the ACA. The ACA algorithm requires $O(rN_s + rN_v) = O(rN_v)$ memory storage and $O(r^2N_s + r^2N_v) = O(r^2N_v)$ CPU time (Zhao et al., 2005). After the matrix compression, the CPU time for constructing the additional excitation matrixes is reduced to $O(rN_v)$. In addition, the computational complexity of the inner solving process is $O(N_s^\alpha \log(N_s))$. Thus, the enhanced solution for the weak coupling case has $O(N_s^\alpha \log(N_s))$ computational complexity.

5 Numerical Results

In this section, numerical results are presented to test the efficiency and validity of the proposed method. The following examples are performed on a personal computer with a 3.70-GHz Intel® Core™ i7-8700K CPU (six cores are used) and 64.0 GB RAM. The computational resources requirements of the direct solution of the GME and the proposed enhanced solution for all numerical results are presented in Table.1. Note that the percentage decrease is obtained by dividing the time and memory reduction of the enhanced solution by the requirements of the direct solution. The iteration steps for the strong coupling cases in Table.1 are derived from the

Table 1 Computational resources requirements of the direct solution and enhanced solution.

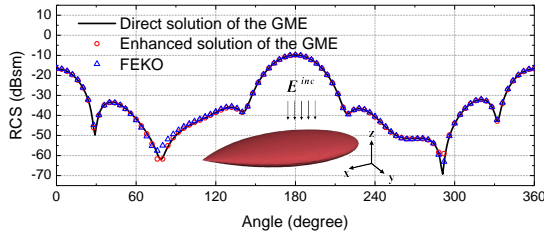
Model			Time (s)			Memory (MB)			Iteration ¹
Name	N_s ²	N_v ³	Direct	Enhanced	Percentage decrease ⁴	Direct	Enhanced	Percentage decrease ⁴	Enhanced
Almond (see Fig.3)	3753	10911	839.20	188.40	77.60	6128.70	1106.70	81.94	77
Stratified ball (see Fig.4)	10833	31652	3370.88	352.04	89.60	24479.00	2705.11	88.90	80
Composite ball (see Fig.5)	21915	72299	45234.50	1546.30	96.60	64879.20	6490.33	90.00	138
Discrete object (see Fig.7)	15404	74423	14008.70	1446.43	89.70	64021.60	5143.57	92.00	79

¹ Iteration: the number of the iteration steps in the enhanced solution.

² N_s : the number of triangle pairs.

³ N_v : the number of tetrahedrons.

⁴ Percentage Decrease: the ratio of the time or memory reduction of the enhanced solution to the direct solution.

**Fig. 3 Bistatic RCS of the almond computed by the direct solution, enhanced solution, and FEKO.**

iterative matrix equation solver, and the iteration steps for the weak coupling case are derived from the coupling process between different sub-regions.

As previously mentioned, the enhanced solution can be used to analyze the scattering characteristic of homogeneous objects. For metal objects, we let $P_c = 1$ and $P_d = 0$ in Eqs (13) and (14). For homogeneous dielectric objects, we let $P_c = 0$ and $P_d = 1$. Here, a dielectric almond shape with relative permittivity (2.0, -0.5) is analyzed first. The object is discretized by 10911 tetrahedrons, which leads to 3753 triangle pairs on its surface. The almond is illuminated by a 3.0 GHz vertically polarized incident plane wave from $(\theta, \phi) = (0^0, 0^0)$. The RCS in the directions $(\theta \in [0^0, 360^0], \phi = 0^0)$ is calculated. Fig.3 shows the RCS result of the enhanced solution compared with the result of the direct solution and the solution using the FEKO software.

Second, two examples are presented to test the accuracy and efficiency of the proposed enhanced solution for the strong coupling case. First, the analysis of a stratified ball is presented. As shown in Fig.4a, 31652 tetrahedrons discretize the ball, and

7222 triangles discretize the boundaries of the sub-regions in total, which leads to 10833 unknowns. The sub-regions formed by dielectric materials A, B, C, D, and the perfect electric conductor (PEC) sub-region contribute 1113, 2307, 3114, 2985, and 1314 unknowns, respectively. The relative error distribution of the total field throughout the dielectric regions with respect to the FEKO solution is presented in Fig.4b. In addition, the relative error is defined by

$$RE(\mathbf{r}) = \frac{|\mathbf{E}^e(\mathbf{r}) - \mathbf{E}^{\text{FEKO}}(\mathbf{r})|}{|\mathbf{E}^{\text{FEKO}}(\mathbf{r})|} \quad (42)$$

where $RE(\mathbf{r})$ is the relative error value at point \mathbf{r} , $\mathbf{E}^e(\mathbf{r})$ is the total field calculated by the proposed enhanced solution, and $\mathbf{E}^{\text{FEKO}}(\mathbf{r})$ is the total field calculated by FEKO, and the norm is defined as the 1-norm form. Then, a composite ball is considered. The composite ball is discretized by 72299 tetrahedrons, and 14610 triangles discretize the boundaries of the sub-regions in sum, which leads to 21915 unknowns. The sub-regions formed by the dielectric materials A, B, C, D, E, and the PEC sub-region contribute 1935, 4086, 4851, 5997, 3972, and 1074 unknowns, respectively as shown in Fig.5a. The total field distribution is presented in Fig.5b. The RCS in directions $(\theta \in [0^0, 360^0], \phi = 0^0)$ for VV polarization calculated by the enhanced solution is in good agreement with the direct solution and the FEKO solution as shown in Fig.6.

Third, a discrete object consisting of several discrete sub-regions is analyzed by the proposed enhanced solution for the weak coupling case. As shown in Fig.7a, the scattering target array is dis-

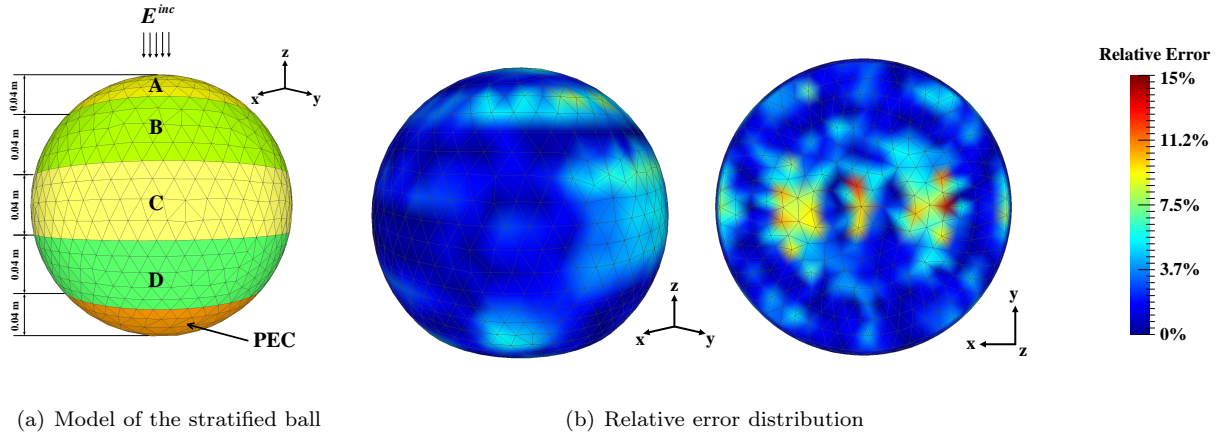


Fig. 4 Model and simulation result of the stratified ball. (a) The ball centered at the origin consists of five sub-regions with the same thickness of 0.04 m. The sub-region at the bottom of the ball is formed by PEC, and the other sub-regions are formed by dielectric materials A, B, C, and D with relative permittivity of 1.5, 2.0, 2.5, and 3.0, respectively. The stratified ball is illuminated by a 1.5 GHz vertically polarized incident wave from $(\theta, \phi) = (0^0, 0^0)$ (b) The relative error distribution among the dielectric sub-regions of the enhanced solution with respect to the FEKO solution.

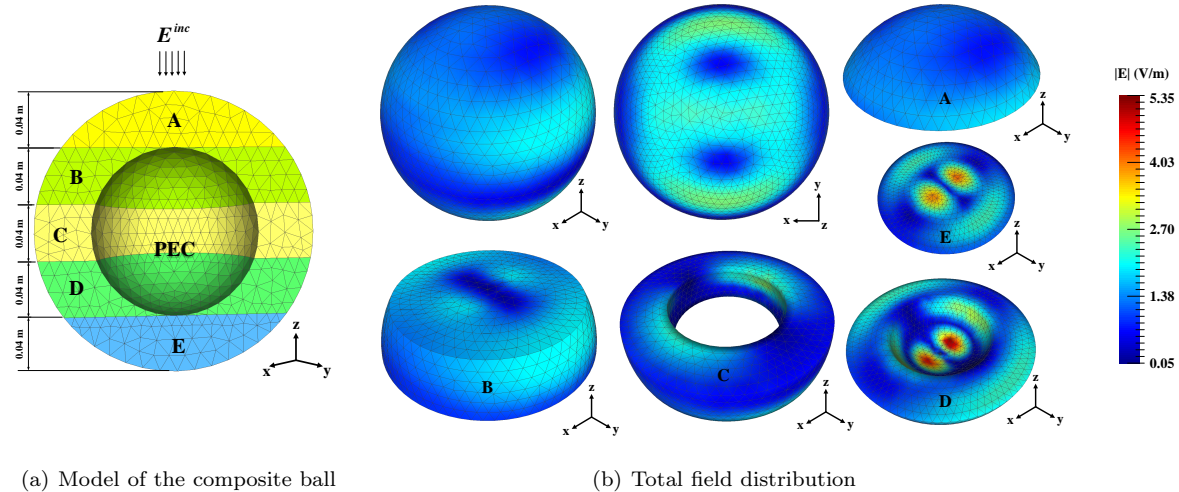


Fig. 5 Model and simulation result of the composite ball. (a) The ball centered at the origin consists of six sub-regions. The inner sphere with a radius of 0.06 m is formed by PEC. The outer layer with a radius of 0.1 m is formed by five dielectric materials A, B, C, D, and E with relative permittivity of 1.5, 2.0, 2.5, 3.0, and 3.5, respectively. The five dielectric sub-regions have the same thickness of 0.04 m. The composite ball is illuminated by a 2.0 GHz vertically polarized incident wave from $(\theta, \phi) = (0^0, 0^0)$. Note that the concave cut is made for improved visibility. (b) The total field distribution of the object is calculated by the enhanced solution. Different views of the dielectric sub-regions are presented.

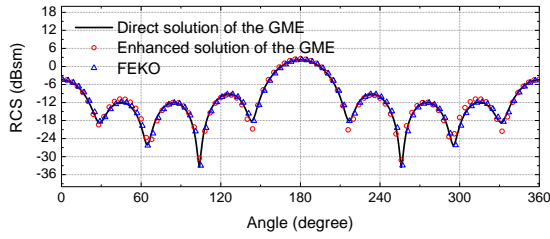


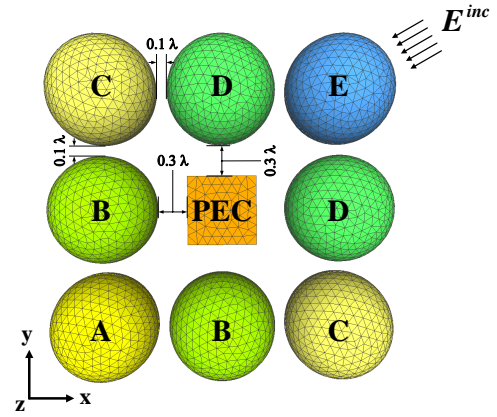
Fig. 6 Bistatic RCS of the composite ball computed by direct solution, enhanced solution, and FEKO.

cretized by 74423 tetrahedrons, and 10276 triangles discretize the boundaries of the sub-regions in total, which leads to 15404 unknowns. The inner PEC cube has 608 unknowns, and the dielectric balls (from the ball formed by material A, counterclockwise) have 1119, 1431, 1860, 2253, 2589, 2253, 1860, and 1431 unknowns. The total field distribution is presented in Fig.7b and Fig.7c. The RCS in directions ($\theta \in [0^\circ, 360^\circ]$, $\phi = 90^\circ$) for VV polarization calculated by the proposed method is in good agreement with the direct solution and the FEKO solution as shown in Fig.8.

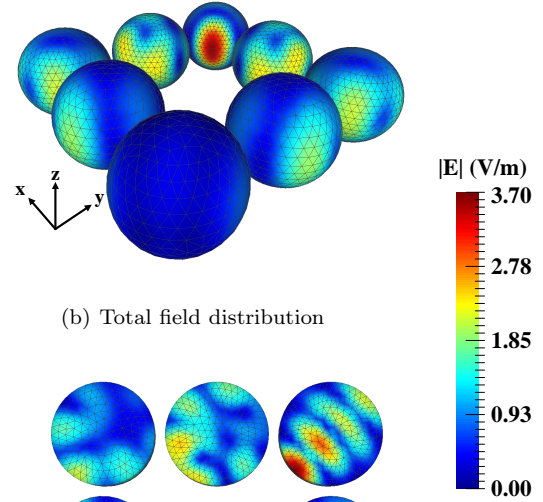
Compared with the direct solution of the GME, the proposed enhanced solution generates results with low relative error, and the proposed method only requires 11.6% memory and 11.8% CPU time on average among these cases. It can be concluded that the enhanced solution has a better performance when analyzing homogeneous objects and composite objects compared with the direct solution.

6 Conclusion

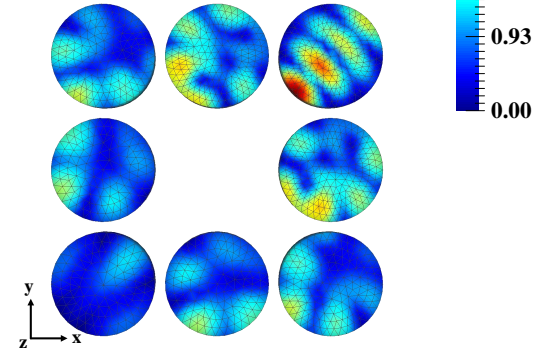
In this paper, an enhanced solution of the SVS-EFIE is proposed and implemented to solve the EM scattering problems of metal-dielectric composite objects. Although the SVS-EFIE can reduce the number of unknowns when analyzing homogeneous dielectric objects, it can result in complex equations, laborious implementation, and unacceptable computational complexity when it is applied to metal-dielectric composite objects. Thus, the GME is first presented to analyze the metal-dielectric composite objects. Note that the GME can also be used to analyze the scattering properties of homogeneous objects. Then, the enhanced solution with two policies is proposed to solve the GME. The two policies can be selected adaptively based on the coupling degree concerning the spacing between different sub-



(a) Model of the discrete object



(b) Total field distribution



(c) Total field distribution

Fig. 7 Model and simulation result of the discrete object. (a) The discrete objects consist of nine sub-regions. The cube in the center with a side length of 0.06 m is formed by PEC. The eight balls with a radius of 0.05 m around the cube are formed by dielectric materials. The dielectric materials A, B, C, D, and E have relative permittivity of 1.5, 2.0, 2.5, 3.0, and 3.5, respectively. The discrete objects are illuminated by a 3.0 GHz vertically polarized incident wave from $(\theta, \phi) = (90^\circ, 45^\circ)$. (b) The total field distribution among the dielectric sub-regions calculated by the enhanced solution. (c) The total field distribution among the dielectric regions on the $z = 0$ plane calculated by the enhanced solution.

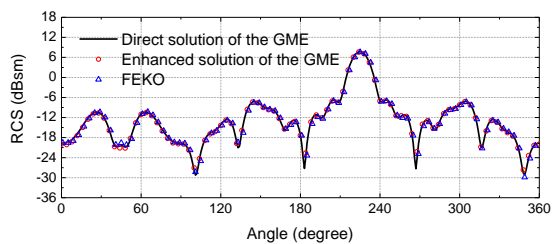


Fig. 8 Bistatic RCS of the discrete object computed by direct solution, enhanced solution, and FEKO.

regions. For the strong coupling case, the enhanced solution based on the addition theorem is proposed. For the weak coupling case, the enhanced solution based on the iterative method and algebra-based matrix compression method is proposed. In addition, CPU parallelism can be easily applied to the enhanced solution. The enhanced solution can obtain results similar to the direct solution, and it requires less memory storage and CPU time. Numerical results demonstrate the efficiency and accuracy of the proposed method.

Contributors (refer to <https://www.casrai.org/credit.html>)

Han Wang designed the research and implemented the software. Ming-jie Pang and Hai Lin processed the data. Han Wang drafted the manuscript. Ming-jie Pang helped organize the manuscript. Han Wang, Ming-jie Pang, and Hai Lin revised and finalized the paper.

Compliance with ethics guidelines

Han Wang, Ming-jie Pang, and Hai Lin declare that they have no conflicts of interest.

References

- Aluru S, Shanker B, Hariharan B, 2002. A scalable parallel fast multipole method for analysis of scattering from perfect electrically conducting surfaces. *SC Conference*, p. 42.
<https://doi.org/10.1109/SC.2002.10012>
- Bucci O, Gennarelli C, Savarese C, 1991. Optimal interpolation of radiated fields over a sphere. *IEEE Transactions on Antennas and Propagation*, 39(11):1633-1643.
<https://doi.org/10.1109/8.102779>
- Chew WC, Michielssen E, Song J, et al., 2001. Fast and Efficient Algorithms in Computational Electromagnetics. Artech House.
- Dagum L, Menon R, 1998. OpenMP: an industry standard api for shared-memory programming. *IEEE Computational Science and Engineering*, 5(1):46-55.
<https://doi.org/10.1109/99.660313>
- Ergul Ö, Gurel L, 2009. Comparison of integral-equation formulations for the fast and accurate solution of scattering problems involving dielectric objects with the multilevel fast multipole algorithm. *IEEE Transactions on Antennas and Propagation*, 57(1):176-187.
<https://doi.org/10.1109/TAP.2008.2009665>
- Gholami R, Okhmatovski V, 2020. Surface-volume-surface EFIE formulation for fast direct solution of scattering problems on general 3-D composite metal-dielectric objects. *IEEE Transactions on Antennas and Propagation*, 68(7):5742-5747.
<https://doi.org/10.1109/TAP.2020.2968762>
- Gholami R, Menshov A, Okhmatovski VI, 2019. \mathcal{H} -matrix accelerated solution of surface-volume-surface EFIE for fast electromagnetic analysis on 3-D composite dielectric objects. *IEEE Journal on Multiscale and Multiphysics Computational Techniques*, 4:152-162.
<https://doi.org/10.1109/JMMCT.2019.2920106>
- Goni O, Okhmatovski VI, 2021. Analytic solution of surface-volume-surface electric field integral equation on dielectric sphere and analysis of its spectral properties. *IEEE Transactions on Antennas and Propagation*, in press.
<https://doi.org/10.1109/TAP.2021.3083829>
- Lu CC, Chew WC, 2000. A coupled surface-volume integral equation approach for the calculation of electromagnetic scattering from composite metallic and material targets. *IEEE Transactions on Antennas and Propagation*, 48(12):1866-1868.
<https://doi.org/10.1109/8.901277>
- Lu CC, 2003. A fast algorithm based on volume integral equation for analysis of arbitrarily shaped dielectric radomes. *IEEE Transactions on Antennas and Propagation*, 51(3):606-612.
<https://doi.org/10.1109/TAP.2003.809823>
- Meagher D, 1982. Geometric modeling using Octree encoding. *Computer Graphics and Image Processing*, 19(2):129-147.
[https://doi.org/https://doi.org/10.1016/0146-664X\(82\)90104-6](https://doi.org/https://doi.org/10.1016/0146-664X(82)90104-6)
- Menshov A, Okhmatovski V, 2013. New single-source surface integral equations for scattering on penetrable cylinders and current flow modeling in 2-D conductors. *IEEE Transactions on Microwave Theory and Techniques*, 61(1):341-350.
<https://doi.org/10.1109/TMTT.2012.2227784>
- Poggio A, Edmund M, 1973. Integral Equation Solutions of Three-dimensional Scattering Problems. MB Assoc., p.159-260.
<https://doi.org/10.1016/B978-0-08-016888-3.50008-8>
- Rao S, Wilton D, Glisson A, 1982. Electromagnetic scattering by surfaces of arbitrary shape. *IEEE Transactions on Antennas and Propagation*, 30(3):409-418.
<https://doi.org/10.1109/TAP.1982.1142818>
- Sarvas J, 2003. Performing interpolation and antinterpolation entirely by fast fourier transform in the 3-D multilevel

- fast multipole algorithm. *SIAM Journal on Numerical Analysis*, 41(6):2180-2196.
<https://doi.org/10.1137/S0036142902405655>
- Sheikh Hosseini Lori F, Menshov A, Gholami R, et al., 2018. Novel single-source surface integral equation for scattering problems by 3-D dielectric objects. *IEEE Transactions on Antennas and Propagation*, 66(2):797-807.
<https://doi.org/10.1109/TAP.2017.2781740>
- Song J, Lu CC, Chew WC, 1997. Multilevel fast multipole algorithm for electromagnetic scattering by large complex objects. *IEEE Transactions on Antennas and Propagation*, 45(10):1488-1493.
<https://doi.org/10.1109/8.633855>
- Song J, Chew WC, 1995. Multilevel fast multipole algorithm for solving combined field integral equation of electromagnetic scattering. *Microwave and Optical Technology Letters*, 10(1):14-19.
<https://doi.org/10.1002/mop.4650100107>
- Xie F, Li W, 2018. A method of VSIE for electromagnetic scattering by planar composite conductor-dielectric structures. 2018 IEEE MTT-S International Wireless Symposium (IWS), p.1-4.
<https://doi.org/10.1109/IEEE-IWS.2018.8400974>
- Zhao K, Vouvakis M, Lee JF, 2005. The adaptive cross approximation algorithm for accelerated method of moments computations of EMC problems. *IEEE Transactions on Electromagnetic Compatibility*, 47(4):763-773.
<https://doi.org/10.1109/TEMC.2005.857898>
- Zheng S, Gholami R, Okhmatovski VI, 2018. Surface-volume-surface electric field integral equation for solution of scattering problems on 3-D dielectric objects in multilayered media. *IEEE Transactions on Microwave Theory and Techniques*, 66(12):5399-5414.
<https://doi.org/10.1109/TMTT.2018.2866855>